High-Gradient Nanomagnets on Cantilevers for Sensitive Detection of Nuclear Magnetic Resonance

Jonilyn G. Longenecker,[†] H. J. Mamin,[‡] Alexander W. Senko,[§] Lei Chen,[†] Charles T. Rettner,[‡] Daniel Rugar,[‡] and John A. Marohn[†,*]

[†]Department of Chemistry and Chemical Biology, Cornell University, Ithaca, New York 14853, United States, [‡]IBM Research Division, Almaden Research Center, San Jose, California 95120, United States, and [§]Department of Materials Science and Engineering, Cornell University, Ithaca, New York 14853, United States

ABSTRACT Detection of magnetic resonance as a force between a magnetic tip and nuclear spins has previously been shown to enable sub-10 nm resolution ^{1}H imaging. Maximizing the spin force in such a magnetic resonance force microscopy (MRFM) experiment demands a high field gradient. In order to study a wide range of samples, it is equally desirable to locate the magnetic tip on the force sensor. Here we report the development of attonewton-sensitivity cantilevers with high-gradient cobalt nanomagnet tips. The damage layer thickness and saturation magnetization of the magnetic material were characterized by X-ray photoelectron spectroscopy and superconducting quantum interference device magnetometry. The coercive field and saturation magnetization of an individual tip were quantified *in situ* using frequency-shift cantilever magnetometry. Measurements of cantilever dissipation *versus* magnetic field and tip—sample separation were conducted. MRFM signals from protons in a polystyrene film were studied *versus* rf irradiation frequency and tip—sample separation, and from this data the tip field and tip-field gradient were evaluated. Magnetic tip performance was assessed by numerically modeling the frequency dependence of the magnetic resonance signal. We observed a tip-field gradient $\partial B_z^{\text{tip}}/\partial z$ estimated to be between 4.4 and 5.4 MT m^{-1}, which is comparable to the gradient used in recent 4 nm resolution ^{1}H imaging experiments and larger by nearly an order of magnitude than the gradient achieved in prior magnet-on-cantilever MRFM experiments.

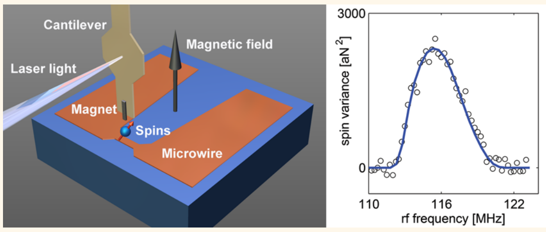

KEYWORDS: nanofabrication · magnetic resonance force microscopy · magnetometry · X-ray photoelectron spectroscopy · superconducting quantum interference device · surface-induced dissipation

The 4 to 10 nm resolution demonstrated by Degen *et al.*[1] in their proton-imaging magnetic resonance force microscopy[2−7] (MRFM) experiment is competitive with the 3 to 8 nm resolution achieved by cryo-electron tomography (cryo-ET) applied to single copies of biomacromolecules[8−11] and approaches the 2 nm resolution often achieved by cryo-electron microscopy (cryo-EM) applied to multiple copies of disordered asymmetric complexes. Given the established importance of cryo-ET and cryo-EM, this resolution comparison suggests that MRFM has an important and complementary role to play in the determination of the structure of single copies of biomacromolecules, biomacromolecular complexes, and other organic nanostructures.

In the most sensitive MRFM experiments to date, signal has been detected as a force variance generated by interactions between the magnetic field gradient produced by a nanomagnet and magnetic dipole fluctuations in a small ensemble of nuclear spins. An attonewton-sensitivity cantilever is used as the force sensor to detect this interaction. In this limit where the force variance is measured, for a given cantilever sensitivity and imaging resolution, the signal acquisition time is dependent on the magnetic tip-field gradient such that the acquisition time is proportional to the inverse of the field gradient to the fourth power.[12] To achieve high-sensitivity MRFM detection, it is thus critical to use a high-gradient magnetic tip.

In the three-dimensional MRFM imaging experiment of ref 1, a magnetic tip with a field gradient of 4.2 MT m^{-1} was achieved by fabricating a 200 nm diameter Fe$_{70}$Co$_{30}$ pillar on a flat surface.[13] The resultant high-resolution imaging experiments were conducted after affixing an individual tobacco mosaic virus to the leading edge of a high-compliance silicon cantilever. Though this work had unprecedented NMR imaging resolution, few biological samples are as robust as the tobacco mosaic virus, and the "sample-on-cantilever" nature of the experiment precluded the use of cryopreservation techniques.

Switching instead to the "magnet-on-cantilever" geometry would enable the study of a broad range of samples. Delicate biological samples that need to be embedded

* Address correspondence to jam99@cornell.edu.

Received for review July 9, 2012
and accepted October 3, 2012.

10.1021/nn3030628

in a thin film of water and flash frozen to preserve their native structure[8−10,14,15] could be prepared for MRFM using standard methods. Since MRFM can be used to noninvasively reconstruct three-dimensional images, working organic semiconductor devices could also be studied. For both of these applications, and many others, having the sample off of the cantilever is essential.

Positioning the magnet on the cantilever dictates that high-gradient magnets must be fabricated directly on high-compliance cantilevers. Magnet-on-cantilever detection of electron spin resonance (ESR)[16−21] and nuclear magnetic resonance (NMR)[22,23] has been observed in prior MRFM experiments; however, the tips were prepared by ion beam milling, and the achievable magnetic field gradients were limited by ion damage. In practice these tips produced a gradient nearly an order of magnitude smaller than that achieved by Degen and co-workers. Thus nearly 10^4 longer imaging times would be required to achieve the 4 to 10 nm resolution of ref 1 using the best ion-beam-milled tip demonstrated to date.

To avoid ion beam damage, Hickman *et al.* batch-fabricated attonewton-sensitivity cantilevers with integrated 100 nm diameter nickel tips patterned by electron-beam (e-beam) lithography.[24] While these cantilevers were successfully used to detect ESR, the yield was very low and electron energy loss spectroscopy indicated that a significant percentage of the nickel was magnetically inactive, presumably as a result of processing damage. Moreover, the observed dependence of the signal on magnetic field agreed poorly with simulations, indicating that the tips were not behaving as a uniformly magnetized rod. To improve the yield, decrease processing-induced damage, and retain the critical ability to use high-resolution e-beam lithography to define the magnets, Longenecker and co-workers[25] recently introduced a combined batch/serial process for fabricating magnet-tipped attonewton-sensitivity cantilevers. Magnets were defined on a silicon-on-insulator wafer using e-beam lithography and liftoff. The wafer was then processed *en batch* to yield nanomagnet tips protruding from the leading edge of suspended micrometer-scale silicon chips, which were attached serially to the ends of attonewton-sensitivity silicon cantilevers using focused ion beam (FIB) milling and attachment. While this approach produced well-magnetized tips in high yield, magnetic resonance studies were not conducted.

Here we report magnet-on-cantilever detection of NMR using an attonewton-sensitivity cantilever with an integrated cobalt nanomagnet tip. Our tip's magnetic field gradient exceeds previous gradients produced by magnets on cantilevers by at least a factor of 8.[18,19,21,23,26] Remarkably, the tip gradient is comparable to the tip employed in the high-resolution imaging experiment of ref 1. Our results thus demonstrate the potential for achieving 4 to 10 nm resolution proton magnetic resonance imaging with reasonable three-dimensional acquisition times for a wide range of thin-film organic samples.

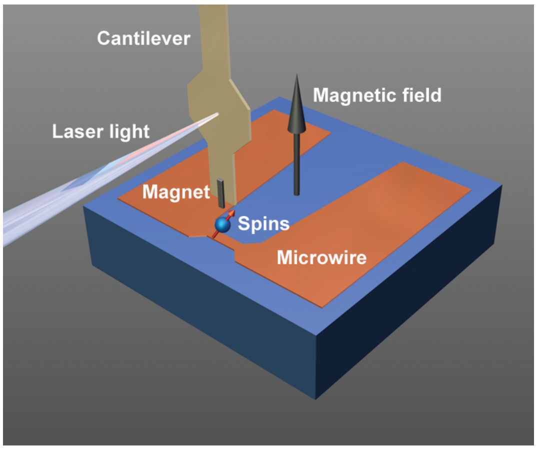

Figure 1. Schematic of the experiment. A cobalt magnet with cross section 225 nm × 79 nm was extended past the leading edge of an attonewton-sensitivity cantilever. The cantilever was centered over a 1 μm wide microwire coated with 40 nm of polystyrene. An external 2.63 T magnetic field was applied in the direction of the long axis of the cantilever as shown. A laser interferometer was centered on a 30 μm wide pad to measure cantilever vibrations.

In the subsequent sections of this paper we detail the fabrication, characterization, and implementation of these high-gradient tips in an NMR-MRFM experiment. To fabricate the e-beam-defined cobalt tips in high yield, the nickel-tip process of ref 25 was revised to avoid high-temperature processing steps. The resulting cobalt-tipped attonewton-sensitivity cantilevers were used to detect stochastic proton magnetization from a polystyrene film spun-cast over a microwire.[27] Artifact-free detection of NMR in this magnet-on-cantilever experiment required substantial modification of the spin-modulation protocols of refs 23 and 1. The spin signal was studied as a function of rf irradiation frequency at multiple tip−sample separations. By modeling this data numerically, the tip field and tip-field gradient were determined. The magnetic integrity of the tip at the nanoscale was assessed by comparing the spin signal to simulations carried out using different damage models. Measurements of force noise as a function of tip−sample separation over a copper microwire and over silicon indicate a larger-than-expected surface noise;[24] we suggest methods for mitigating this surface noise in future experiments.

RESULTS

The experiment is sketched in Figure 1. The magnetic resonance force microscope used here has been described in detail elsewhere.[1,27] Cobalt-tipped cantilevers (Figure 2) were prepared as described in the Methods section. The cantilever used in these experiments had a resonance frequency f_c = 6644 Hz,

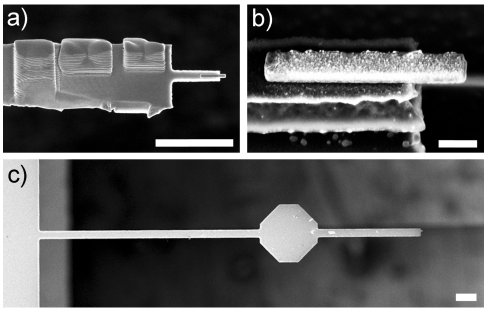

Figure 2. Scanning electron microscope images of the magnet-tipped cantilever used in the MRFM experiment. (a) Top-view image of the magnet-tipped chip attached to an underlying cantilever by ion-assisted platinum deposition; three rectangular platinum patches can be seen on the top side of the chip. The cobalt magnet is seen to overhang a 3 μm long finger at the leading edge of the chip. Scale bar = 5 μm. (b) Angled image of the overhanging cobalt nanomagnet, acquired before it was attached to a cantilever. The magnet was 225 ± 15 nm wide, 1494 ± 15 nm long, and 79 ± 4 nm thick. There was a 4 nm titanium layer under the magnet to promote adhesion to the silicon substrate, as well as an 8 nm platinum capping layer to mitigate oxidation. Scale bar = 200 nm. (c) Top-view image of a custom-fabricated 200 μm long cantilever drawn from the same batch as the cantilever used in this experiment. Scale bar = 20 μm.

an intrinsic quality factor $Q = 8.4 \times 10^4$ *in vacuo*, and a spring constant $k = 1.0$ mN m^{-1}.

The magnetic integrity of the tips was examined using a combination of characterization techniques. X-ray photoelectron spectroscopy (XPS), in conjunction with argon ion milling, was used to measure the elemental composition *versus* depth in 80–100 nm thick cobalt films prepared on silicon substrates. All films had a 4 nm titanium adhesion underlayer, and some films were capped with an 8 nm thick protective platinum coating. To estimate the damage incurred by subsequent processing, films were compared with and without exposure to elevated temperatures; baked films were coated with (poly)methylmethacrylate (PMMA) resist and heated at 115 °C for 40 min (the PMMA was removed using solvent prior to XPS analysis). Unbaked films without protective platinum coatings measured oxygen within the first 3 nm of the cobalt layers; baking the material caused an additional 2–5 nm of oxidation for a total oxidation depth of 5–8 nm (Supporting Information, Figure S2). The platinum capping layer successfully eliminated the surface oxidation in both unbaked and baked films (Supporting Information, Figure S3). Superconducting quantum interference device (SQUID) magnetometry indicated that platinum-capped cobalt films exhibited saturation magnetizations close to the theoretical saturated magnetic moment for cobalt of 1.8 T (Supporting Information, Figure S5).

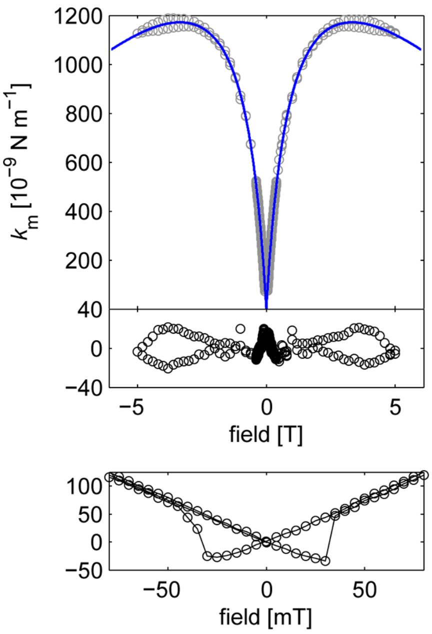

Figure 3. A frequency-shift cantilever magnetometry study of the cobalt nanomagnet used in this experiment. The external field was swept from +5 to −5 T and then back from −5 to +5 T. Upper: Magnetic spring constant shift k_m *versus* field (open circles) and a best fit to eq 1 (solid line). Middle: Fit residuals. Lower: Magnified view of the spring constant hysteresis observed at low field.

The magnetic integrity of the individual cobalt nanomagnet at the cantilever leading edge (Figure 2b) was verified *in situ* prior to MRFM measurements using frequency-shift cantilever magnetometry. The observed cantilever frequency shift Δf was converted to an equivalent magnet-induced spring constant shift using $k_m = 2k\Delta f/f_c$. The resulting data between −5.0 to −0.05 T and 0.05 to 5.0 T were fit to[28,29]

$$k_m(B) = \mu_{sat}\left(\frac{\alpha}{l}\right)^2 \frac{B\Delta B}{B+\Delta B} + c|B| \qquad (1)$$

with $B = \mu_0 H$ the applied magnetic field, $\alpha = 1.377$ a constant for the fundamental cantilever mode, $l = 200$ μm the cantilever length, and μ_{sat} the saturated magnetic moment. Here $\Delta B = \mu_0 \mu_{sat} \Delta N/V$ is the shape-anisotropy field, with V the tip volume and $\Delta N = N_t - N_l$ the difference in demagnetization factor along the cantilever's thickness and length, respectively. The last term in eq 1 approximately accounts for the field-dependent spring constant shift of the bare cantilever at high field.[29,30] The measured magnetic moment was converted to saturation magnetization using $\mu_0 M_{sat} = \mu_0 \mu_{sat}/V$ with $V = 225$ nm × 1494 nm × 79 nm.

The measured $k_m(B)$ data shown in Figure 3 were well described by eq 1. The observed $\Delta N = 0.56 \pm 0.01$ was in reasonable agreement with the 0.50 expected for a high-aspect-ratio prolate ellipsoid. The observed saturation magnetization $\mu_0 M_{sat} = 1.91 \pm 0.03$ T agreed well with the 1.80 T expected for cobalt. Here we report the standard error in $\mu_0 M_{sat}$ as an indication of the goodness of fit; the true error in $\mu_0 M_{sat}$ is dominated by the uncertainly in k, which we caution could be 40% or larger. Taken together with the XPS and SQUID data on large-area thin films, these findings strongly support the conclusion that the tip exhibits a saturation magnetization close to the expected value for a fully intact cobalt nanomagnet.

To detect nuclear magnetic resonance, the magnet-tipped cantilever was centered over the microwire and brought into close proximity to the polystyrene film coating the microwire surface (Figure 1). The amplitude and frequency of the rf delivered to the microwire were modulated to induce cyclic inversions of the proton spins. To avoid spurious signal, a new spin modulation protocol, COZMIC (compensated zero mean inversion cycles), was implemented, as described in the Methods section. A spin variance signal was inferred by subtracting in-phase and out-of-phase force fluctuations acting on the cantilever.

In Figure 4 we display measured spin variance signal $\sigma_{\mathrm{spin}}{}^2$ (open circles) as a function of the rf center frequency (f_{rf}) at five tip−sample separations (h) ranging from 42.3 to 13.1 nm. We observe that for each tip−sample separation the low-frequency edge of the signal is constant at a frequency of 112 MHz, whereas the high-frequency edges increase in rf frequency as the tip is brought closer to the sample. Both of these observations are well understood. The spin variance signal arises from protons in the sample that meet the resonance condition $f_{\mathrm{rf}} = (\gamma_{\mathrm{p}}/2\pi)|\mathbf{B}^{\mathrm{ext}} + \mathbf{B}^{\mathrm{tip}}(\mathbf{r})|$, with $\gamma_{\mathrm{p}}/2\pi$ = 42.56 MHz/T the gyromagnetic ratio for protons, $\mathbf{B}^{\mathrm{ext}}$ the applied magnetic field, and $\mathbf{B}^{\mathrm{tip}}(\mathbf{r})$ the magnetic field generated by the cobalt nanomagnet at location **r**. The low-frequency edge of each signal shown in Figure 4 arises from spins far away from the tip where the magnetic field contribution from the tip is nearly zero. For $|\mathbf{B}^{\mathrm{ext}}|$ = 2.63 T, such "bulk" spins should meet the magnetic resonance condition at a frequency f_{l} = 2.63 T × 42.56 MHz/T = 112 MHz, as we observed. The high-frequency edge of the signal arises from spins close to the cantilever experiencing an additional magnetic field from the cobalt nanomagnet. Due to the cobalt tip's field gradient, the field experienced by the spins at the surface increases as the tip−sample separation is reduced.

The tip field and vertical tip-field gradient of the cobalt nanomagnet were estimated as a function of tip−sample separation by matching the shape of the experimental data in Figure 4a−e to simulated spin variances. In the simulations, the sample was assumed to be a 40 nm thick polystyrene film and the magnet had dimensions identical to the magnet shown in Figure 2b. Details of the simulation parameters are provided in the Supporting Information.

Agreement between the simulations and the experimental data was obtained after considering several tip models. When simulations were conducted for a fully saturated cobalt nanomagnet, the tip field was overestimated by more than a factor of 2 (Supporting Information, Figure S6). Thus, damage models had to be considered. Magnet parameters using two models were optimized to match the shape of the spin variance signal and accurately estimate the tip field. In the first model (method 1), the magnet was assumed to have a magnetic spacing that was 51 nm larger than the measured tip−sample separation. The spin variance signals calculated using this extraneous spacing of 51 nm are overlaid with the experimental data in Figure 4 as the blue lines. Using method 1, the nanomagnet's tip field B_z^{tip} was calculated as a function of tip−sample separation (Figure 5; blue dot-dashed line), and numerical differentiation was used to calculate the tip-field gradient $\partial B_z^{\mathrm{tip}}/\partial z$ (Figure 5; green dashed line). From the tip-field gradient plot in Figure 5, we can see that at the smallest tip−sample separation of 13.1 nm the vertical tip-field gradient was calculated to be 4.4 MT m^{-1} for spins directly below the cobalt nanomagnet. In the second damage model (method 2), the extraneous spacing was set to zero, but the saturated magnetic moment for the nanomagnet was reduced from 1.8 T to 0.69 T. Method 2 provided a quality of fit that was almost as good as that for method 1. Using method 2, the vertical tip-field gradient was estimated as 5.4 MT m^{-1} for a tip−sample separation of 13.1 nm.

A comparison of the results obtained using method 1 and method 2 indicates to us that a number of tip

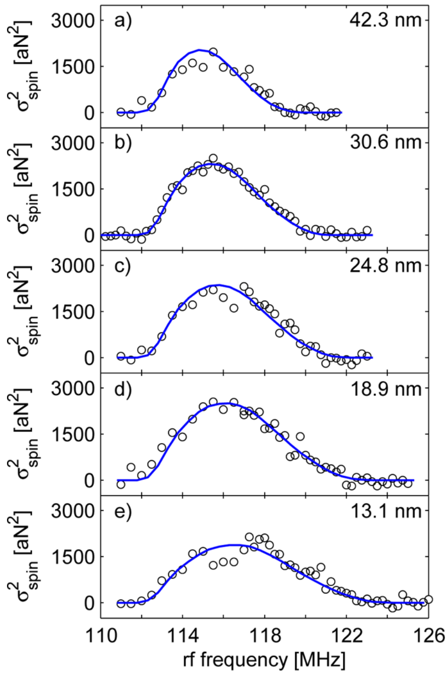

Figure 4. Magnetic resonance signal of protons in a 40 nm thick polystyrene film. The experimental spin variance signal $\sigma_{\mathrm{spin}}{}^2$ (open circles) was obtained by measuring the spin-induced force fluctuations experienced by a cobalt nanomagnet affixed to an attonewton-sensitivity cantilever that was brought into close proximity to the film. Signal was obtained at tip−sample separations of (a) 42.3 nm, (b) 30.6 nm, (c) 24.8 nm, (d) 18.9 nm, and (e) 13.1 nm. The static field was 2.63 T, and the peak-to-peak rf frequency deviation Δf_{FM} was 2 MHz. Simulated spin variance signals (blue lines) were calculated at each tip−sample separation assuming a rectangular cuboid magnet with an extraneous spacing of 51 nm (method 1).

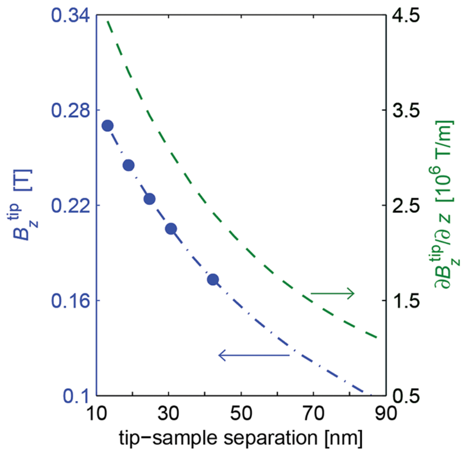

Figure 5. Tip field B_z^{tip} (left axis; blue) and tip-field gradient $\partial B_z^{\text{tip}}/\partial z$ (right axis; green) of the cobalt nanomagnet. As shown in Figure 4, a damage model for a tip with an extraneous spacing of 51 nm was used to calculate spin variance signal as a function of rf frequency. This model was used to determine B_z^{tip} as a function of tip−sample separation (blue dot-dashed line) by calculating the difference between the high-frequency and low-frequency edges of the simulated signal at 15 different spacings. The five calculated tip fields that correspond to the tip−sample separations in Figure 4 are shown as blue filled circles. The tip-field gradient for the cobalt nanomagnet at the same 15 tip−sample separations (green dashed line) was determined by numerically differentiating the tip fields.

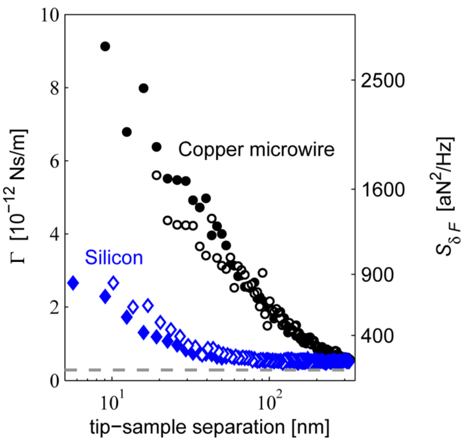

Figure 6. Cantilever dissipation Γ (left axis) *versus* tip−sample separation and the corresponding spectral density of force fluctuations $S_{\delta F}$ at $T = 5.5$ K (right axis). Dissipation is shown for the tip centered over the copper microwire (black circles) and over the silicon substrate (blue diamonds). Measurements were conducted at $B^{\text{ext}} = 2.63$ T (solid circles and diamonds) and at zero field (open circles and diamonds). The dotted gray line is the cantilever's internal dissipation, calculated from the cantilever f_c, k, and Q measured far away from the surface.

damage scenarios could reproduce the data within experimental error but estimate somewhat different tip-field gradients. As a check, we thus also tested a model-free method (method 3) for estimating the tip field and tip-field gradient as follows. The downward-sloping peak data in each curve were fit to a line and the frequency (f_h) of the high-frequency edge was obtained from the *x*-intercept of the line. The *z*-component of the tip field was calculated as $B_z^{\text{tip}} = (f_h - f_1)/(\gamma_p/2\pi)$. The tip-field gradient was obtained by computing the derivative of the tip-field data numerically; computing the tip-field gradient using the $h = 13.1$ and 18.9 nm data points gave the estimate $\partial B_z^{\text{tip}}/\partial z = 5.1$ MT m^{-1}. Because of the curvature of the slope of the simulated signal, we expect method 3 to underestimate the tip field.

The friction coefficient (Γ) experienced by the magnet-tipped cantilever was studied over both the (polystyrene-coated) copper microwire and the (polystyrene-coated) silicon substrate at tip−sample separations ranging from 5 to 300 nm. Measurements were conducted at 2.63 T and at zero field over both surfaces. The corresponding spectral density of force fluctuations at the cantilever frequency was calculated from the measured friction coefficient using $S_{\delta F} = 4k_B T\Gamma$ with k_B being Boltzmann's constant and $T = 5.5$ K the temperature. The resulting data are displayed in Figure 6. For comparison, the cantilever's calculated internal friction coefficient is also shown; the cantilever's intrinsic properties were used to calculate that $\Gamma = k/(2\pi f_c Q) = 2.85 \times 10^{-13}$ Ns/m and that the associated thermally limited force noise spectral density was 9.3 aN Hz$^{-1/2}$. The dissipation over the silicon substrate remained close to the thermal limit until a separation of approximately 100 nm. In contrast, the dissipation over the microwire became surface limited at tip−sample separations below 280 nm. The dissipation over both locations was essentially independent of applied magnetic field.

Larger-than-expected cantilever frequency fluctuations were also observed over both the silicon substrate and the copper microwire (Supporting Information, Figure S7). Over silicon, the spectral density of cantilever frequency fluctuations ($S_{\delta f_c}$) shows a low-frequency 1/*f* tail indicative of dielectric fluctuations in silicon or polystyrene.[31,32] The $S_{\delta f_c}$ over the microwire, in contrast, shows large spikes that suggest noise arising from mechanical vibrations.[33]

DISCUSSION

The data presented in Figure 4 and Figure 5 are the main results of this work. We demonstrated the successful detection of spin variance signal from protons in a magnet-on-cantilever MRFM experiment and found a vertical tip-field gradient on the order of 5 MT m^{-1}.

Method 1 and method 2 (described in the Results section) provide relevant lower and upper bounds for the vertical tip-field gradient of the cobalt nanomagnet. In method 1 the damage is modeled for the worst-case scenario in which all damage is concentrated at the magnet−sample interface. This extraneous spacing effectively increases the tip−sample separation and would most strongly reduce the tip-field gradient experienced by spins closest to the magnet's physical leading edge. Alternately, the damage is spread evenly throughout the entire magnet in method 2, which allows for the retention of interactions between sample spins and magnetic material as close as the measured tip−sample separation of 13.1 nm. For a tip−sample separation of 13.1 nm, method 1 and method 2 were used to calculate vertical tip-field gradients of 4.4 and 5.4 MT m^{-1}, respectively. As expected, the gradient estimated using method 1 is the lower value.

To understand which, if either, of these simulated models correctly predicts the damage that led to the experimentally observed reduction in the tip field, we characterized the integrity of the cobalt material using XPS depth profiling, SQUID magnetometry, and *in situ* cantilever magnetometry. Results indicated that unprotected cobalt surfaces oxidized to a thickness of less than 10 nm and that the rest of the cobalt remained fully intact. A simulation-free method for estimating the tip-field gradient was also used to compare to the results of method 1 and method 2; this method estimated that $\partial B_z^{\text{tip}}/\partial z \geq 5.1$MT m^{-1}. The gradient predicted by method 1 is thus lower than expected, and the assumption in method 2 that the damage is uniformly spread through the nanomagnet is in stark contrast with the less than 10 nm of damage expected based on the characterization measurements. On the basis of these findings, both of our simulation methods are likely oversimplifications of the true damage scenario. The simulation results taken together with the cobalt material characterization indicate that the discrepancy between the expected and observed tip fields may be due to a combination of (1) oxidation of all unprotected cobalt surfaces to a depth of 10 nm, (2) surface roughness on the magnet leading edge and sample film, and (3) a protrusion of the titanium underlayer past the cobalt leading edge.

While the nanomagnet's gradient is outstanding, the dissipation experienced by the magnet-tipped cantilever is disappointingly high, particularly near the microwire. At tip−sample separations of $h \leq 20$ nm, the intrinsic force sensitivity of 9 aN $\text{Hz}^{-1/2}$ degraded to 40 aN $\text{Hz}^{-1/2}$ over the polymer-coated microwire and to 20 aN $\text{Hz}^{-1/2}$ over the polymer-coated silicon substrate. This behavior is in striking contrast with Hickman *et al.*, whose cantilever with a similarly sized nickel tip maintained a force sensitivity of 10 aN $\text{Hz}^{-1/2}$ down to $h \leq 3$ nm over a gold-coated polymer film.[24] Comparing the two experiments is instructive. In the Hickman *et al.* experiment, Γ was measured at zero field over a gold-coated polystyrene film spun on top of an ac-coupled gold half-wave microwave resonator, and the tip potential was adjusted to minimize Γ. Here, in contrast, the tip was brought over a dc-coupled copper microwire at high magnetic field, the sample covering the microwire was not metal coated, and it was not possible to adjust the tip potential to null the contact potential difference between the tip and the substrate.

There are two general dissipation mechanisms to consider: (1) tip magnetization coupling to fluctuating magnetic field gradients in the substrate, equivalent *via* the fluctuation−dissipation theorem to eddy current damping,[17,34,35] and (2) tip charge coupling to fluctuating electric field gradients in the substrate.[36−39] One might expect the eddy current damping to be stronger in a high external field where the tip is fully magnetized, whereas we instead observed Γ to be largely field independent. However, SQUID measurements revealed the magnetic film to have significant remanence (Supporting Information, Figure S5), which would lead to eddy current damping even at zero field. Now consider damping arising from fluctuating electric field gradients. There are certainly stray electrostatic fields between the tip and substrate at small separations due to both differences in the overall work functions and work function inhomogeneities. Previous room-temperature dissipation measurements[6,36,37] have shown sizable differences between dissipation over metal layers and over polymer films due to electrostatic/dielectric effects; these same effects may be partly responsible for the roughly 4 times difference between the dissipation on and off the microwire. Still, since both the silicon and the microwire were covered with the same polymer, we suspect that the dominant dissipation source was magnetic.

For a tip−sample separation of 13.1 nm and under the signal averaging conditions of ref 1, our magnet-tipped cantilevers are projected to achieve a resolution of 5 to 10 nm. Assuming that we are dominated by eddy current damping, a simple solution to improve the dissipation and further enhance the achievable resolution could be to increase the sample thickness or introduce a dielectric spacer between the microwire and the sample.

CONCLUSION

In summary, we have produced magnet-tipped attonewton-sensitivity cantilevers and have used them to detect nuclear magnetic resonance with $\leq 500\ \mu_{\text{p}}$ sensitivity. The tip-field gradient of 4.4 to 5.4 MT m^{-1} observed here is comparable to the 4.2 MT m^{-1} field gradient produced by the $Fe_{70}Co_{30}$ pillar in the sample-on-cantilever experiment of ref 1 and is 8 to 10 times larger than the best tip gradient demonstrated to date in a magnet-on-cantilever MRFM experiment.[18]

That such a large gradient can be achieved in a magnet-on-cantilever MRFM experiment is an exciting advance. It should enable the characterization of as-fabricated semiconductor devices, for example, where Stark shifts of magnetic resonance transitions[40−42] allow the measurement of internal electric fields in semiconductor devices containing quadrupolar nuclei.[43−45] We moreover anticipate that moving the sample off-cantilever will allow the full battery of cryo-EM sample preparation techniques[14,15] to be applied in an MRFM experiment to prepare fragile biomolecules, macromolecular complexes, and thin sections of biological material. In contrast with cryo-EM, MRFM can accommodate micrometer-thick samples, and image contrast can be achieved by isotopic labeling, which is nonperturbative. MRFM's present resolution of 4 to 10 nm is competitive with what has been demonstrated in cryo-ET studies of subcellular structures,[46] organelles,[47] neuronal synapses,[48] and viral synapses[49] where studying a single copy of the structure is essential. When multiple, precisely identical copies of a highly symmetric and large macromolecule or macromolecular complex are available, cryo-EM with single particle analysis can achieve near-atomic resolution. Frustratingly, broad classes of trafficking agents such as exosomes[50] and membrane proteins remain difficult to study by cryo-EM because the associated macromolecules or macromolecular complexes are disordered, have molecular weights less than 100 kDa,[51] or simply do not retain their native structure in aqueous solution. With only slightly improved resolution, we anticipate that the type of magnet-on-tip magnetic resonance force microscope demonstrated here can begin to contribute to our understanding of such important biological nanostructures.

METHODS

Measurements were conducted in high vacuum ($P < 10^{-6}$ mbar) with the temperature maintained at $T = 5.5$ K. In all experiments reported here, both the sample and the cantilever were electrically grounded. In the following paragraphs we summarize the procedures used to produce the magnet-tipped cantilevers and study their tip magnetization *in situ* using frequency-shift cantilever magnetometry. We also summarize the protocols used to prepare the sample, detect nuclear magnetic resonance, and study cantilever dissipation.

Cantilever Fabrication. Cantilevers were fabricated from single-crystal silicon-on-insulator (SOI) wafers as described by Jenkins *et al.*[52] and Hickman *et al.*[24] The silicon orientation was ⟨100⟩, the device silicon thickness was 340 nm, the device silicon resistivity was 14 to 22 Ω cm, and the buried oxide thickness was 400 nm. The resulting cantilevers were 4 μm wide and 200 μm long and had a 30 μm wide reflective pad centered 70 μm from the leading edge (Figure 2c). Separately, cobalt nanomagnets were fabricated on silicon chips prepared from identical SOI wafers. The original protocol for the fabrication of nickel-tipped chips is described in ref 25; here an overview of the process is provided and required modifications to enable compatibility with cobalt nanomagnets are detailed. Etch slits were defined in the SOI wafer's device layer, and the resulting chips were released using a buffered oxide etch prior to deposition of the nanomagnets. The magnets were defined using e-beam lithography in bilayer (poly)methylmethacrylate resist and deposited by e-beam evaporation. The nanomagnets were prepared by depositing a titanium adhesion layer (4.0 ± 0.2 nm thick; deposited at 1.5 Å/s), cobalt (79.2 ± 4.7 nm; 2.9 Å/s), and a platinum capping layer (8.0 ± 0.5 nm; 1.2 Å/s). Relative metal thicknesses were measured during deposition by a quartz crystal microbalance, and the combined thickness of the Ti/Co/Pt film was measured after fabrication by atomic force microscopy. Silicon under the leading 300 nm of the magnets was removed by patterning U-shaped holes[24,25] in a layer of 700 nm thick, $M_w = 4.95 \times 10^5$ PMMA resist immediately in front of the magnet and isotropically etching the silicon using a sulfur hexafluoride and oxygen (SF_6:O_2) plasma. In order to prevent oxidation of the cobalt magnets, it was critical to bake the PMMA at only 115 °C. Scanning electron microscope (SEM) images of the magnet-tipped chip and overhanging magnet are shown in Figure 2a and b, respectively. An FEI Strata 400 STEM dual focused ion beam system was used to serially attach the magnet-tipped chips to cantilevers.[25] Compared with our prior work, the shape of the chips has been improved to facilitate their attachment to the cantilever (see Supporting Information, Figure S1). Magnet-tipped cantilevers were prepared at Cornell University four weeks before they were transferred to the MRFM apparatus at IBM Almaden Research Center. They were exposed to ambient air for approximately five days, were stored under nitrogen for three days, and were otherwise stored under a vacuum of 10^{-4} mbar.

Cantilever Characterization. A representative cantilever is shown in the SEM image in Figure 2c. The magnet-tipped cantilever used in this study had a resonance frequency $f_c = 6644$ Hz, an intrinsic quality factor $Q = 8.4 \times 10^4$ *in vacuo*, and a spring constant $k = 1.0$ mN m^{-1}. Cantilever displacement was monitored with a low-power[53] temperature-tuned[54] fiber-optic interferometer ($\lambda = 1550$ nm, $P \approx 25$ nW). The interferometer output was sent to a field programmable gate array (FPGA), which was used to either control the cantilever Q *via* negative feedback[55] or self-oscillate the cantilever to a set amplitude *via* positive feedback.[56] The output of the FPGA drove a piezoelectric disk at the base of the cantilever holder. The cantilever spring constant was determined from the mean square displacement of the undriven cantilever at a temperature $T = 5.5$ K;[57] a correction factor was used to account for the distance from the reflective pad to the end of the cantilever. Based on the ±15 μm uncertainty in the position of the laser, we estimate that the error in k could be as large as ±40%. To study cantilever dissipation, the cantilever ringdown time τ was measured and a cantilever quality factor and dissipation constant were calculated using $Q = \tau\pi f_c$ and $\Gamma = k/(2\pi f_c Q)$, respectively. The cantilever amplitude was set to 15 nm when measuring dissipation during approach. To study cantilever frequency noise, the instantaneous frequency of the self-oscillated cantilever was determined by fitting short, 4 ms segments of the digitized cantilever oscillation to a sine wave; the power spectral density of cantilever frequency fluctuations was computed from the resulting frequency *versus* time data. For these studies a cantilever peak-to-peak amplitude of 60 nm was chosen because it approximated the ideal amplitude for detecting a single spin at a tip−sample separation of 23 nm in a force-gradient experiment, assuming a spherical tip radius of 41 nm.[6] To determine the location of the sample surface, the tip−sample separation h was decreased until a dc deflection of the cantilever was observed. The displacement per volt of the vertical piezoelectric actuator was calibrated *via* fiber-optic interferometry, and the distance above this “touch point” was computed from the piezo voltage taking into account this (temperature-dependent) piezo calibration. The estimated error in h is ±3 nm.

Magnetic Material Characterization. The integrity of the cantilever's cobalt nanomagnet was analyzed *in situ* using frequency-shift cantilever magnetometry.[24,25,28−30] The cantilever was mechanically driven into self-oscillation, and the cantilever frequency was monitored as the field was swept from +5 to −5 T and then back from −5 to +5 T. Methods used to prepare and analyze magnetic thin-film samples using superconducting quantum interference device magnetometry and X-ray photoelectron spectroscopy are detailed in the Supporting Information.

Sample and Microwire Preparation. A lithographically defined copper microwire was used to generate magnetic radiofrequency fields.[1,27] The microwire was prepared on a silicon substrate as described in ref 27, but with the magnetic pillar omitted. The sample consisted of a thin film of polystyrene prepared from solution *via* spin coating. Polystyrene powder (Pressure Chemical, $M_w = 2.0 \times 10^5$, $M_w/M_n = 1.06$) was dissolved in toluene to a final concentration of 0.3 wt %, and the resulting solution was spun onto a 4 mm × 4 mm silicon-plus-microwire substrate rotating at 6000 rpm. The high rotation speed and low viscosity resulted in a reasonably uniform film in spite of edge effects and the substrate's topographic features. The film's solvent was removed *via* air drying. Using FIB milling and SEM, the final film thickness was estimated to be 40 nm.

Spin Detection Protocol. Statistical fluctuations in proton magnetization were observed following the general approach of Degen *et al.*[58] Cyclic inversions of the sample magnetization were induced by triangle-wave rf sweeps with peak-to-peak FM deviation Δf_{FM} = 2 MHz. The resulting cantilever motion was detected with a two-channel lock-in amplifier. The strength of the applied rf field was $B_1 \cong 5$ mT. The proton magnetization fluctuated with a correlation time of τ_m = 100 to 150 ms; to accurately capture the induced cantilever position fluctuations, the cantilever response time was adjusted *via* feedback to be approximately 15 ms. The lock-in outputs were converted to units of force, and a spin signal was computed from the variance of the outputs using $\sigma_{spin}^2 = \sigma_x^2 - \sigma_y^2$, where σ_x^2 and σ_y^2 represent the variances of the in-phase and quadrature lock-in signals, respectively. For most data points in Figure 4, the spin variance signal was computed from 12.5 min of lock-in data per rf frequency step. For the 117 to 126 MHz data at the three smallest tip−sample separations, $h \leq 25$ nm, the spin variance signal was computed from 16.7 min of lock-in data per rf frequency step.

In prior sample-on-cantilever experiments,[1] optimized spin inversions were obtained using rf that was both frequency modulated (swept unidirectionally twice per cantilever cycle) and amplitude modulated (ramped to zero when the rf frequency was maximally off-resonance). In our magnet-on-cantilever experiment, however, we found that this modulation scheme caused a parametric amplification of thermomechanical noise in one lock-in channel, yielding a false spin signal. This false variance imbalance was eliminated by operating the rf continuously and using triangle-wave frequency modulation. The triangle-wave frequency modulation, however, produced a spurious oscillation of the cantilever, which in practice exhibited variations that obscured the spin signal.

Using our detection protocol COZMIC, we solved this problem by adding a small amount of amplitude modulation back into the rf so as to just cancel any spurious cantilever excitation caused by the frequency modulation (FM). This cancellation was accomplished by measuring the mean cantilever amplitude with the lock-in amplifier and applying a sinusoidal amplitude modulation (AM) to exactly cancel the mean cantilever excitation. The frequency-modulated rf waveform was multiplied by $1 + A\cos(2\pi f_c t) + B\sin(2\pi f_c t)$, where A and B are small numbers that control the amplitude compensation. The in-phase and quadrature lock-in outputs X and Y were measured for two trials of amplitude compensation, and a complex-number transfer function was computed from $\chi \approx (\Delta X + i\Delta Y)/(\Delta A + i\Delta B)$. Knowing the transfer function, one can precisely predict how much amplitude modulation to apply to cancel the mean signal. After every 50 s of MRFM data collection and every time the cantilever was moved to a new location, we (1) measured the cantilever frequency, (2) computed a triangle FM waveform using the old values of A and B for AM compensation, (3) remeasured the lock-in mean for 5 s to determine the average X and Y, (4) calculated new values for A and B using the transfer function and the measured values for X and Y, (5) updated the triangle FM waveform using the new A and B values, (6) measured the mean lock-in outputs for 5 s and calculated an updated transfer function for future use, (7) measured the MRFM signal for 50 s, and (8) repeated. This compensation scheme worked precisely and automatically.

Conflict of Interest: The authors declare no competing financial interest.

Acknowledgment. The authors thank M. Sherwood for assistance with polymer sample preparation, J. Shu for assistance with the collection and interpretation of XPS data, and B. Carragher and C. Potter for helpful discussions. This research was funded by the National Science Foundation through the Cornell Center for Nanoscale Systems (Grant Nos. EEC-0117770 and EEC-0646547; J.G.L.), the National Institutes of Health (Grant No. 5R01GM-070012; A.W.S., L.C., J.A.M.), the Army Research Office (Grant No. W911NF-09-C-0073; H.J.M., D.R.), and the Army Research Office MultiUniversity Research Initiative (Grant No. W911NF-05-1-0403; J.G.L., J.A.M.). This work made use of facilities in the Cornell Center for Materials Research (CCMR), supported by the National Science Foundation Materials Research Science and Engineering Centers (MRSEC) program (Grant No. DMR-0520404). This work also was performed in part at the Cornell NanoScale Facility, a member of the National Nanotechnology Infrastructure Network, which is supported by the National Science Foundation (Grant No. ECS-0335765).

Supporting Information Available: Magnet-tipped chip additional details, XPS methods and findings, SQUID methods and findings, cantilever frequency noise data, and a comparison with previous high-gradient tips. This material is available free of charge *via* the Internet at http://pubs.acs.org.

REFERENCES AND NOTES

1. Degen, C. L.; Poggio, M.; Mamin, H. J.; Rettner, C. T.; Rugar, D. Nanoscale Magnetic Resonance Imaging. *Proc. Natl. Acad. Sci. U. S. A.* **2009**, *106*, 1313–1317.
2. Sidles, J. A. Noninductive Detection of Single-Proton Magnetic Resonance. *Appl. Phys. Lett.* **1991**, *58*, 2854–2856.
3. Rugar, D.; Yannoni, C. S.; Sidles, J. A. Mechanical Detection of Magnetic Resonance. *Nature* **1992**, *360*, 563–566.
4. Rugar, D.; Züger, O.; Hoen, S.; Yannoni, C. S.; Vieth, H.-M.; Kendrick, R. D. Force Detection of Nuclear Magnetic Resonance. *Science* **1994**, *264*, 1560–1563.
5. Sidles, J. A.; Garbini, J. J.; Bruland, K. J.; Rugar, D.; Züger, O.; Hoen, S.; Yannoni, C. S. Magnetic Resonance Force Microscopy. *Rev. Mod. Phys.* **1995**, *67*, 249–265.
6. Kuehn, S.; Hickman, S. A.; Marohn, J. A. Advances in Mechanical Detection of Magnetic Resonance. *J. Chem. Phys.* **2008**, *128*, 052208.
7. Poggio, M.; Degen, C. L. Force-Detected Nuclear Magnetic Resonance: Recent Advances and Future Challenges. *Nanotechnology* **2010**, *21*, 342001.
8. Zhou, Z. H. Towards Atomic Resolution Structural Determination by Single-Particle Cryo-Electron Microscopy. *Curr. Opin. Struct. Biol.* **2008**, *18*, 218–228.
9. Tocheva, E. I.; Li, Z.; Jensen, G. J. Electron Cryotomography. *Cold Spring Harbor Perspect. Biol.* **2010**, *2*, a003442–a003442.
10. Orlova, E. V.; Saibil, H. R. Structural Analysis of Macromolecular Assemblies by Electron Microscopy. *Chem. Rev.* **2011**, *111*, 7710–7748.
11. Zhang, L.; Ren, G. IPET and FETR: Experimental Approach for Studying Molecular Structure Dynamics by Cryo-Electron Tomography of a Single-Molecule Structure. *PLoS ONE* **2012**, *7*, e30249.
12. Mamin, H. J.; Rettner, C. T.; Sherwood, M. H.; Gao, L.; Rugar, D. High Field-Gradient Dysprosium Tips for Magnetic Resonance Force Microscopy. *Appl. Phys. Lett.* **2012**, *100*, 013102.
13. Here we report the revised gradient estimate used in ref 12.
14. Grassucci, R. A.; Taylor, D. J.; Frank, J. Preparation of Macromolecular Complexes for Cryo-Electron Microscopy. *Nat. Protoc.* **2007**, *2*, 3239–3246.
15. Marko, M.; Hsieh, C.; Schalek, R.; Frank, J.; Mannella, C. Focused-Ion-Beam Thinning of Frozen-Hydrated Biological Specimens for Cryo-Electron Microscopy. *Nat. Methods* **2007**, *4*, 215–217.
16. Wago, K.; Botkin, D.; Yannoni, C. S.; Rugar, D. Paramagnetic and Ferromagnetic Resonance Imaging with a Tip-on-Cantilever Magnetic Resonance Force Microscope. *Appl. Phys. Lett.* **1998**, *72*, 2757–2759.
17. Stipe, B. C.; Mamin, H. J.; Yannoni, C. S.; Stowe, T. D.; Kenny, T. W.; Rugar, D. Electron Spin Relaxation near a Micron-Size Ferromagnet. *Phys. Rev. Lett.* **2001**, *87*, 277602.
18. Mamin, H. J.; Budakian, R.; Chui, B. W.; Rugar, D. Detection and Manipulation of Statistical Polarization in Small Spin Ensembles. *Phys. Rev. Lett.* **2003**, *91*, 207604.

19. Rugar, D.; Budakian, R.; Mamin, H. J.; Chui, B. W. Single Spin Detection by Magnetic Resonance Force Microscopy. *Nature* **2004**, *430*, 329–332.
20. Moore, E. W.; Lee, S.-G.; Hickman, S. A.; Wright, S. J.; Harrell, L. E.; Borbat, P. P.; Freed, J. H.; Marohn, J. A. Scanned-Probe Detection of Electron Spin Resonance from a Nitroxide Spin Probe. *Proc. Natl. Acad. Sci. U. S. A.* **2009**, *106*, 22251–22256.
21. Fong, K. C.; Herman, M. R.; Banerjee, P.; Pelekhov, D. V.; Hammel, P. C. Spin Lifetime in Small Ensembles of Electron Spins Measured by Magnetic Resonance Force Microscopy. *Phys. Rev. B* **2011**, *84*, 220405.
22. Garner, S. R.; Kuehn, S.; Dawlaty, J. M.; Jenkins, N. E.; Marohn, J. A. Force-Gradient Detected Nuclear Magnetic Resonance. *Appl. Phys. Lett.* **2004**, *84*, 5091–5093.
23. Mamin, H. J.; Budakian, R.; Chui, B. W.; Rugar, D. Magnetic Resonance Force Microscopy of Nuclear Spins: Detection and Manipulation of Statistical Polarization. *Phys. Rev. B* **2005**, *72*, 024413.
24. Hickman, S. A.; Moore, E. W.; Lee, S.-G.; Longenecker, J. G.; Wright, S. J.; Harrell, L. E.; Marohn, J. A. Batch-Fabrication of Cantilevered Magnets on Attonewton-Sensitivity Mechanical Oscillators for Scanned-Probe Nanoscale Magnetic Resonance Imaging. *ACS Nano* **2010**, *4*, 7141–7150.
25. Longenecker, J. G.; Moore, E. W.; Marohn, J. A. Rapid Serial Prototyping of Magnet-Tipped Attonewton-Sensitivity Cantilevers by Focused Ion Beam Manipulation. *J. Vac. Sci. Technol. B* **2011**, *29*, 032001.
26. Bruland, K. J.; Dougherty, W. M.; Garbini, J. L.; Sidles, J. A.; Chao, S. H. Force-Detected Magnetic Resonance in a Field Gradient of 250000 T per Meter. *Appl. Phys. Lett.* **1998**, *73*, 3159–3161.
27. Poggio, M.; Degen, C. L.; Rettner, C. T.; Mamin, H. J.; Rugar, D. Nuclear Magnetic Resonance Force Microscopy with a Microwire RF Source. *Appl. Phys. Lett.* **2007**, *90*, 263111.
28. Marohn, J. A.; Fainchtein, R.; Smith, D. D. An Optimal Magnetic Tip Configuration for Magnetic-Resonance Force Microscopy of Microscale Buried Features. *Appl. Phys. Lett.* **1998**, *73*, 3778–3780.
29. Stipe, B. C.; Mamin, H. J.; Stowe, T. D.; Kenny, T. W.; Rugar, D. Magnetic Dissipation and Fluctuations in Individual Nanomagnets Measured by Ultrasensitive Cantilever Magnetometry. *Phys. Rev. Lett.* **2001**, *86*, 2874–2877.
30. Ng, T. N.; Jenkins, N. E.; Marohn, J. A. Thermomagnetic Fluctuations and Hysteresis Loops of Magnetic Cantilevers for Magnetic Resonance Force Microscopy. *IEEE Trans. Magn.* **2006**, *42*, 378–381.
31. Yazdanian, S. M.; Hoepker, N.; Kuehn, S.; Loring, R. F.; Marohn, J. A. Quantifying Electric Field Gradient Fluctuations over Polymers Using Ultrasensitive Cantilevers. *Nano Lett.* **2009**, *9*, 2273–2279.
32. Yazdanian, S. M.; Marohn, J. A.; Loring, R. F. Dielectric Fluctuations in Force Microscopy: Noncontact Friction and Frequency Jitter. *J. Chem. Phys.* **2008**, *128*, 224706.
33. Hoepker, N.; Lekkala, S.; Loring, R. F.; Marohn, J. A. Quantifying Dielectric Fluctuations over Polymer Films Using an Atomic Force Microscope. *J. Phys. Chem. B* **2011**, *115*, 14493–14500.
34. Sidles, J. A.; Garbini, J. L.; Dougherty, W. M.; Chao, S.-H. The Classical and Quantum Theory of Thermal Magnetic Noise, with Applications in Spintronics and Quantum Microscopy. *Proc. IEEE* **2003**, *91*, 799–816.
35. Giorgio, M.; Meier, B.; Magin, R.; Meyer, E. Magnetic Damping Losses of Tipped Cantilevers. *Nanotechnology* **2006**, *17*, 871–880.
36. Stipe, B. C.; Mamin, H. J.; Stowe, T. D.; Kenny, T. W.; Rugar, D. Noncontact Friction and Force Fluctuations between Closely Spaced Bodies. *Phys. Rev. Lett.* **2001**, *87*, 096801.
37. Kuehn, S.; Loring, R. F.; Marohn, J. A. Dielectric Fluctuations and the Origins of Noncontact Friction. *Phys. Rev. Lett.* **2006**, *96*, 156103.
38. Kuehn, S.; Marohn, J. A.; Loring, R. F. Noncontact Dielectric Friction. *J. Phys. Chem. B* **2006**, *110*, 14525–14528.
39. Labaziewicz, J.; Ge, Y.; Leibrandt, D. R.; Wang, S. X.; Shewmon, R.; Chuang, I. L. Temperature Dependence of Electric Field Noise above Gold Surfaces. *Phys. Rev. Lett.* **2008**, *101*, 180602.
40. Gill, D.; Bloembergen, N. Linear Stark Splitting of Nuclear Spin Levels in GaAs. *Phys. Rev.* **1963**, *129*, 2398–2403.
41. Dixon, R. W.; Bloembergen, N. Electrically Induced Perturbations of Halogen Nuclear Quadrupole Interactions in Polycrystalline Compounds. I. Phenomenological Theory and Experimental Results. *J. Chem. Phys.* **1964**, *41*, 1720–1738.
42. Dixon, R. W.; Bloembergen, N. Electrically Induced Perturbations of Halogen Nuclear Quadrupole Interactions in Polycrystalline Compounds. II. Microscopic Theory. *J. Chem. Phys.* **1964**, *41*, 1739–1749.
43. Marohn, J. A.; Carson, P. J.; Hwang, J. Y.; Miller, M. A.; Shykind, D. N.; Weitekamp, D. P. Optical Larmor Beat Detection of High-Resolution Nuclear Magnetic Resonance in a Semiconductor Heterostructure. *Phys. Rev. Lett.* **1995**, *75*, 1364–1367.
44. Kempf, J. G.; Weitekamp, D. P. Method for Atomic-Layer-Resolved Measurement of Polarization Fields by Nuclear Magnetic Resonance. *J. Vac. Sci. Technol. B* **2000**, *18*, 2255–2262.
45. Kempf, J. G.; Miller, M. A.; Weitekamp, D. P. Imaging Quantum Confinement with Optical and POWER (Perturbations Observed with Enhanced Resolution) NMR. *Proc. Natl. Acad. Sci. U. S. A.* **2008**, *105*, 20124–20129.
46. Milne, J. L. S.; Subramaniam, S. Cryo-Electron Tomography of Bacteria: Progress, Challenges and Future Prospects. *Nat. Rev. Microbiol.* **2009**, *7*, 666–675.
47. Frey, T. G.; Perkins, G. A.; Ellisman, M. H. Electron Tomography of Membrane-Bound Cellular Organelles. *Annu. Rev. Biophys. Biomol. Struct.* **2006**, *35*, 199–224.
48. Fernandez-Busnadiego, R.; Schrod, N.; Kochovski, Z.; Asano, S.; Vanhecke, D.; Baumeister, W.; Lucic, V. Insights into the Molecular Organization of the Neuron by Cryo-Electron Tomography. *J. Electron Microsc.* **2011**, *60*, S137–S148.
49. Felts, R. L.; Narayan, K.; Estes, J. D.; Shi, D.; Trubey, C. M.; Fu, J.; Hartnell, L. M.; Ruthel, G. T.; Schneider, D. K.; Nagashima, K.; *et al.* 3D Visualization of HIV Transfer at the Virological Synapse between Dendritic Cells and T Cells. *Proc. Natl. Acad. Sci. U. S. A.* **2010**, *107*, 13336–13341.
50. Mathivanan, S.; Fahner, C. J.; Reid, G. E.; Simpson, R. J. ExoCarta 2012: Database of Exosomal Proteins, RNA and Lipids. *Nucleic Acids Res.* **2011**, *40*, D1241–D1244.
51. Wu, S.; Avila-Sakar, A.; Kim, J.; Booth, D.; Greenberg, C.; Rossi, A.; Liao, M.; Li, X.; Alian, A.; Griner, S.; *et al.* Fabs Enable Single Particle cryoEM Studies of Small Proteins. *Structure* **2012**, *20*, 582–592.
52. Jenkins, N. E.; DeFlores, L. P.; Allen, J.; Ng, T. N.; Garner, S. R.; Kuehn, S.; Dawlaty, J. M.; Marohn, J. A. Batch Fabrication and Characterization of Ultrasensitive Cantilevers with Submicron Magnetic Tips. *J. Vac. Sci. Technol. B* **2004**, *22*, 909–915.
53. Mamin, H.; Rugar, D. Sub-Attonewton Force Detection at Millikelvin Temperatures. *Appl. Phys. Lett.* **2001**, *79*, 3358–3360.
54. Bruland, K. J.; Garbini, J. L.; Dougherty, W. M.; Chao, S. H.; Jensen, S. E.; Sidles, J. A. Thermal Tuning of a Fiber-Optic Interferometer for Maximum Sensitivity. *Rev. Sci. Instrum.* **1999**, *70*, 3542–3544.
55. Jacky, J. P.; Garbini, J. L.; Ettus, M.; Sidles, J. A. Digital Control of Force Microscope Cantilevers Using a Field Programmable Gate Array. *Rev. Sci. Instrum.* **2008**, *79*, 123705.
56. Albrecht, T. R.; Grütter, P.; Horne, D.; Rugar, D. Frequency Modulation Detection Using High-Q Cantilevers for Enhanced Force Microscope Sensitivity. *J. Appl. Phys.* **1991**, *69*, 668–673.
57. Hutter, J. L.; Bechhoefer, J. Calibration of Atomic-Force Microscope Tips. *Rev. Sci. Instrum.* **1993**, *64*, 1868–1873.
58. Degen, C. L.; Poggio, M.; Mamin, H. J.; Rugar, D. Role of Spin Noise in the Detection of Nanoscale Ensembles of Nuclear Spins. *Phys. Rev. Lett.* **2007**, *99*, 250601.